ACS APPLIED MATERIALS & INTERFACES
Research Article
www.acsami.org

A Novel Method to Synthesize Highly Photoactive Cu_2O Microcrystalline Films for Use in Photoelectrochemical Cells

Changli Li,[†] Yanbo Li,[‡] and Jean-Jacques Delaunay*,[†]

[†]School of Engineering, The University of Tokyo, 7-3-1 Hongo, Bunkyo-ku, Tokyo 113-8656, Japan
[‡]Department of Chemical System Engineering, The University of Tokyo, 7-3-1 Hongo, Bunkyo-ku, Tokyo 113-8656, Japan

Supporting Information

ABSTRACT: Large-scale and high-quality Cu_2O microcrystalline films with high photoactivity are synthesized using a novel and low-cost method. The enhanced photoactivity is achieved through the formation of Cu_2O microcrystalline films having well-defined crystal facets and porous structure. Cu_2O microcrystalline films are fabricated by decomposing previously synthesized $Cu(OH)_2$ nanowires on a Cu foil under a vacuum. Subsequent crystal growth during the annealing process is driven by outward diffusion of Cu ions and oxidation. Crystal growth induces coalescence of the nanowires and results in the formation of Cu_2O microcrystals enclosed by four {111} facets. Photoelectrochemical evaluation of the annealed samples performed under chopped simulated AM 1.5G illumination reveals that the sample annealed at 500 °C for 2 h exhibited the highest photocurrent of 4.07 mA/cm^2 at 0 V/RHE. This large photocurrent is ascribed to a high carrier density ($\sim 1.36 \times 10^{18}$ cm^{-3}) and a low carrier transfer resistance in electrolyte, as evidenced by electrochemical impedance spectroscopy. The obtained low-cost Cu_2O microcrystalline film (2 h) may serve as an excellent solar absorber and carrier provider for use in photovoltaics and artificial photosynthesis.

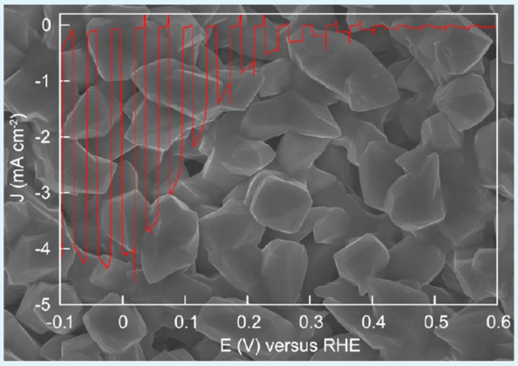

KEYWORDS: *Cu_2O microcrystalline film, Cu vacancies, photoactivity, photoelectrochemical cell*

1. INTRODUCTION

Cuprous oxide (Cu_2O) is a well-known metal-deficit p-type semiconductor with holes as the charge carriers.[1,2] The direct energy bandgap of 1.9−2.5 eV makes it a promising material for solar energy conversion. In addition, the position of the conduction band (more negative than −0.7 V vs RHE) provides a large driving force for proton reduction in photoelectochemical cells.[3−5] Thus, Cu_2O has been used as a visible light catalyst for H_2 production from water,[6−10] as an electrocatalyst for CO_2 reduction,[11] and as a high open-circuit voltage solar cell in the configuration of conventional solid state[12] or semiconductor/liquid junctions.[13]

Electrodeposition[3−5,14] and thermal oxidation of Cu[1,2] are the two most common methods for the fabrication of Cu_2O films. Several studies on Cu_2O photocathodes for water splitting prepared by electrodeposition showed that water can hardly be split at Cu_2O via a normal photocatalytic reaction[3−5,14] and under some conditions the observed small photocurrent can be attributed to the reduction of oxygen in the solution.[3,4] The low photoactivity of those Cu_2O polycrystalline films and powder may be due to the low carrier density and inefficient charge transport, thus limiting the overall water splitting performances when Cu_2O was used in combination with other n-type materials.[6,14] However, by controlling the electrodeposition parameters (e.g., temperature and pH) properly, Paracchino et al.[5] reported a high photocurrent of 2.4 mA/cm^2 at 0.25 V vs RHE for a bare Cu_2O film under AM 1.5G illumination. Although part of the current originated from the reduction of Cu_2O to Cu, highly active and stable photocathodes for H_2 production were obtained after coating Cu_2O by protective layers.[7,15,16] Similarly, the PEC performance of the unstable Cu_2O electrodes with a high photocurrent of about 2.28 mA/cm^2 at 0 V vs RHE prepared by thermal annealing of $Cu(OH)_2$ can also be optimized by carbon coating.[10] Coating of the bare Cu_2O with appropriate protective layers is essential for efficient and stable water splitting, and the photoactivity of Cu_2O is crucial for the efficiency of the Cu_2O/protective layer structure.

In this report, a highly photoactive Cu_2O microcrystalline film exhibiting a considerably large photocurrent of 4.07 mA/cm^2 (0 V vs RHE) in PEC measurement under standardized AM 1.5 light illumination was obtained. Cu_2O films were prepared by thermal decomposition of $Cu(OH)_2$ nanowires under a proper annealing pressure at 500 °C. The Cu_2O film morphology was continuously modified with the annealing time. The Cu_2O film annealed for 2 h achieved the highest photocurrent as well as the largest carrier density ($\sim 1.36 \times 10^{18}$ cm^{-3}) compared to the 1, 3, and 4 h samples. The high photoactivity and robust Cu_2O film may serve as an excellent

Received: October 14, 2013
Accepted: December 3, 2013
Published: December 3, 2013

dx.doi.org/10.1021/am404527q | *ACS Appl. Mater. Interfaces* 2014, 6, 480−486

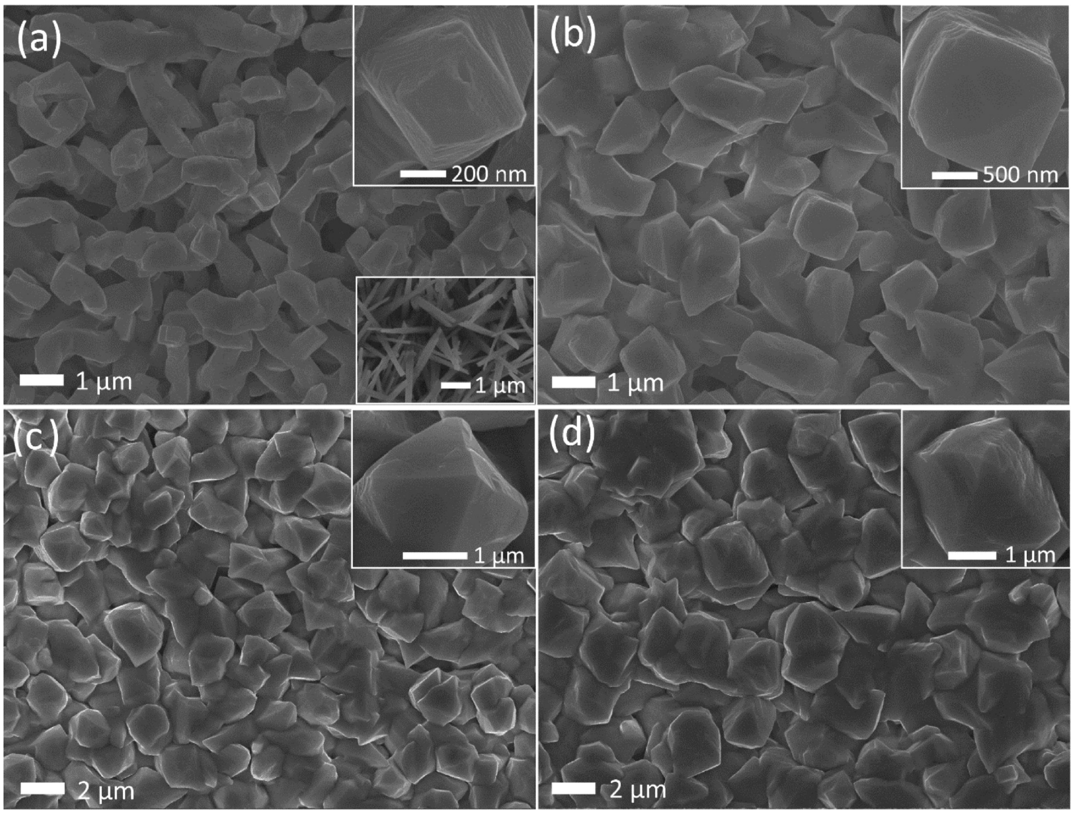

Figure 1. FE-SEM images of the Cu_2O films prepared at 500 °C with different annealing times. (a−d) Cu_2O microcrystalline films prepared at 500 °C for 1, 2, 3, and 4 h, respectively. The top right insets in all images are the enlarged images of the microcrystal, and the lower right inset in part a is the $Cu(OH)_2$ nanowires before annealing.

substrate for light absorption and carrier provider for the application of photoelectrolysis and photovoltaics.

2. EXPERIMENTAL SECTION

2.1. Fabrication of $Cu(OH)_2$ Nanowires. The $Cu(OH)_2$ nanowires were grown on a Cu foil using a simple and scalable wet chemical method.[17] A typical fabrication process was performed as follows. The Cu foil (99.96%, Nilaco) with a size of 10 × 10 mm^2 and a thickness of 0.2 mm was cleaned sequentially in acetone and ethanol ultrasonic bath for 10 min. The cleaned Cu foil was then immersed into a solution containing 2.67 M NaOH (97.0%, Wako) and 0.133 M $(NH_4)_2S_2O_8$ (98.0%, Wako) for 10 min. In addition, gentle stirring of the solution at low temperature (5 °C) was implemented to prevent the formation of CuO flowers on the $Cu(OH)_2$ nanowires. CuO flowers were found to grow under the conditions of inhomogeneous solution and increase in temperature near the Cu/solution interface caused by the chemical reaction. Finally, the Cu foil with a light blue color was taken out from the solution, rinsed with deionized water, and dried in air.

2.2. Fabrication of Cu_2O Microcrystalline Films. The Cu_2O microcrystalline films were prepared by annealing the $Cu(OH)_2$ nanowire film at 500 °C for different times under an Ar atmosphere. More specifically, the $Cu(OH)_2$ nanowires/Cu foil were loaded into an alumina boat and placed at the center of a quartz tube. The quartz tube was evacuated to about 36 Pa before heating, and the flow rate of Ar was 50 sccm during the annealing. The working pressure during the annealing was kept at about 2.5×10^3 Pa. The $Cu(OH)_2$ nanowires/Cu samples were annealed at 500 °C for 1, 2, 3, and 4 h to obtain Cu_2O microcrystalline films with different morphologies.

2.3. Photoelectrochemical and Electrochemical Impedance Measurements. The photoelectrochemical performance of the Cu_2O electrodes was performed in a three-electrode configureuration using an Ag/AgCl reference electrode and a Pt wire counter electrode. The electrolyte was a 0.5 M Na_2SO_4 solution with a pH of 6. Before the measurements, the Na_2SO_4 solution was stirred and purged with Ar gas for 10 min. The photoresponse was measured under chopped AM 1.5G simulated sunlight corresponding to an irradiance of 100 mW/cm^2. The scan rate for the linear sweep voltammetry was 10 mV/s.

The electrochemical impedance measurements of the Cu_2O films were carried out under dark conditions using a potentiostat (VersaSTAT 4, Princeton Applied Research) with an AC amplitude of 10 mV and a frequency of 1 kHz. An aqueous solution of 0.01 M PBS (phosphate buffer saline, pH 7.4) was used as the electrolyte.

2.4. Structural Characterization. The morphology of the samples was characterized by using a field-emission scanning electron microscope (JEOL JSM 7600FA). The X-ray diffraction (XRD) patterns were determined using a diffractometer (Miniflex II-MW, Rigaku Co. Ltd., Japan) with Cu Kα radiation. The Raman spectra of the samples were measured with a Renishaw inVia Raman Microscope system using 488 nm excitation light directed through a ×20 objective with 1.21 mW for top surface analysis and ×100 objective with 0.1 mW for cross-section analysis. The UV−vis diffuse reflectance spectra were determined with a spectrophotometer (DRS, V-560, Jasco).

3. RESULTS AND DISCUSION

3.1. Morphology of the Structures. The $Cu(OH)_2$ nanowires were prepared on a Cu foil by a wet chemical method in sodium hydroxide and ammonium solution, as reported previously.[17] The synthesized $Cu(OH)_2$ nanowires, shown in the lower right inset of Figure 1a, have a diameter of approximately 200 nm and a length of about 5 μm. The XRD pattern (Figure S1, Supporting Information) indicates that only $Cu(OH)_2$ and Cu peaks can be found in the $Cu(OH)_2$ nanowires/Cu structure. After annealing in an Ar atmosphere at 500 °C, the $Cu(OH)_2$ nanowires were completely transformed into Cu_2O by dehydration of $Cu(OH)_2$ into CuO at about 120 °C and further removal of oxygen from CuO, leading to the formation of Cu_2O at higher temperature.[18] The sample morphology was found to continuously vary with the annealing time. The nanowires coalesced to larger crystals, and the size of the crystals increased with annealing time. Parts a−d of Figure 1 show the SEM images of Cu_2O films prepared under Ar atmosphere at 500 °C for 1, 2, 3, and 4 h, respectively. For the 1 h sample shown in Figure 1a, it is found that the neighboring nanowires merge into larger micro-nano aggregates (~0.5 μm) having their tips enclosed by four incomplete {111} facets. For the longer annealing time of 2 h, larger microcrystals are observed and their mean size increases to 1.5 μm, as shown in Figure 1b. The inset of Figure 1b is evidence for the formation of some microcrystals completely covered by smooth {111} facets. When the annealing time is further increased to 3 h (Figure 1c), the size of the microcrystals was increased to 2 μm and most of the crystals display a four {111} facets tip (inset of Figure 1c). At the longest time (4 h, Figure 1d), irregular microcrystals with a size of about 2.5 μm were observed, which indicates that a long annealing time at 500 °C degrades the regularity of the crystals to some extent. The formation of the microcrystals was presumably induced by an appropriate oxygen partial pressure during the annealing process. Indeed, the base pressure (36 Pa) in the vacuum furnace is relatively high compared to other results obtained in high-vacuum annealing systems.[8−10] To confirm the effect of the oxygen partial pressure, we annealed the $Cu(OH)_2$ nanowires in a high-vacuum chamber (~10^{-5} Pa) at 500 °C for 3 h and found that the nanowire structure was not changed; that is, no morphology reconstruction was observed (Figure S2, Supporting Information), in agreement with previous reports.[8−10] The mechanism of the surface reconstruction coalescence may be explained as follows. For low O_2 partial pressure, the high temperature annealing (~500 °C) will only separate the oxygen from the lattice of CuO to form Cu_2O and the stress resulting from the phase change bends the nanowires, as shown in Figure S2a (Supporting Information). For high O_2 partial pressure, the temperature and oxygen partial pressure of this experiment are considered to be in the region of stability of Cu_2O according to the phase diagram.[19] Thus, besides the removal of oxygen from the lattice of CuO to form Cu_2O, the growth of the Cu_2O layer proceeds under this pressure by outward diffusion of Cu ions from the Cu substrate via Cu vacancies to the oxide/oxygen interface and reacts with the oxygen from the gas phase.[2,20,21] The oxidation reaction on the surface leads to a volume expansion of the nanowires and consequently coalescence of the nanowires. Finally, large crystals enclosed by low surface energy facets {111} are formed in order to minimize the total surface energy of the system.[22] The thickness of the oxide layers was estimated to be 7.5, 18.5, 28, and 37 μm for the annealing times of 1, 2, 3, and 4 h, respectively. In summary, subsequent growth of the Cu_2O crystals from nanowires induces oxide growth along the nanowires so that the grown crystals offer well-defined exposed crystal facets as well as clear separation between each crystal, providing a large surface area for chemical reaction.

3.2. XRD and Raman Characterization. The XRD patterns of the Cu_2O microcrystalline films prepared at 500 °C for different annealing times are shown in Figure 2. The results suggest the coexistence of two types of Cu_2O phases in the films. For the 1 h annealed sample, two sets of diffraction peaks are clearly seen and the diffraction peaks are well indexed to the peaks of the cubic structure Cu_2O-I (indicated by dashed line, space group Pn-3m, lattice constant 4.2600 Å, ICDD PDF card No. 1010941) and the Cu_2O-II (indicated by solid line, space group Pn-3m, lattice constant 4.2685 Å, ICDD PDF card No. 9007497). As the annealing time increases, the intensity of the Cu_2O-I peaks decreases and simultaneously the intensity of the Cu_2O-II peaks increases. For an annealing time of 4 h and judging from the XRD pattern, the sample was completely transformed into the Cu_2O-II phase. The change of the intensity of Cu peaks may be explained by the outward diffusion of Cu ions from the Cu foil to the oxide layer. The outward diffusion of Cu ions should be supported by the gradient of Cu vacancies between the oxide/oxygen interface (high concentration) and the Cu/oxide interface (low concentration).[2,20,21] In addition to the outward lattice diffusion of Cu ions under high temperature (above 800−900 °C), grain-boundary diffusion becomes relevant at low annealing temperature (500 °C).[23,24] Thus, diffusion through the lattice may account for the continuous increase in the Cu_2O oxide layer,[24] whereas Cu ions via grain-boundary diffusion may accumulate and form Cu grains embedded in the oxide layer as detected by XRD. When the annealing time increases from 1 to 2 h, the increase in the Cu peaks may be due to the continuous migration of Cu ions through the Cu_2O grain-boundary and thus more Cu grains accumulated in the Cu_2O layer. With further increase in the annealing time (3 and 4 h), the thickness of the oxide layer increases further and the grain-boundary diffusion should become limited by long range transport, so that the intensity of the Cu_2O peaks increases and the intensity of the Cu peaks decreases.

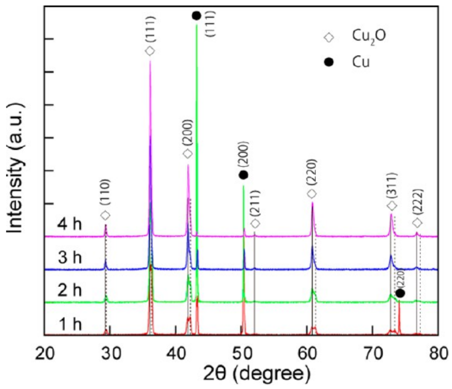

Figure 2. XRD patterns of the Cu_2O samples obtained by annealing the $Cu(OH)_2$ nanowires at 500 °C for 1, 2, 3, and 4 h. The two phases of Cu_2O are indexed using the ICDD PDF card nos. 9007497 and 1010941 and indicated by the solid line and dashed line, respectively.

The phase transformation was further confirmed by Raman spectroscopy. The crystal structure of Cu_2O is a cubic lattice with six atoms in the primitive unit cell and belongs to the *Pn*-3*m* space group. In a perfect Cu_2O lattice, only the peaks from ${}^3\Gamma_{25}{}^+$ (Raman active) and 2 ${}^3\Gamma_{15}{}^-$ (infrared active) can be observed. However, several Raman scattering studies reported the relaxation of the selection rules resulting from impurity in non-stoichiometric Cu_2O.[25] Figure 3c shows the Raman spectra taken from the top surface of the Cu_2O films prepared with different annealing times. The characteristic peaks can be identified as follows:[25] the lines at 148, 626, and 649 cm^{-1} are essentially attributed to the intrinsic $\Gamma_{15}{}^-$ infrared-allowed (IR) active modes; the lines observed at 412 and 496 cm^{-1} are interpreted as originating in double-photon processes; the line at 217 cm^{-1} corresponds to the activation of the zone edge

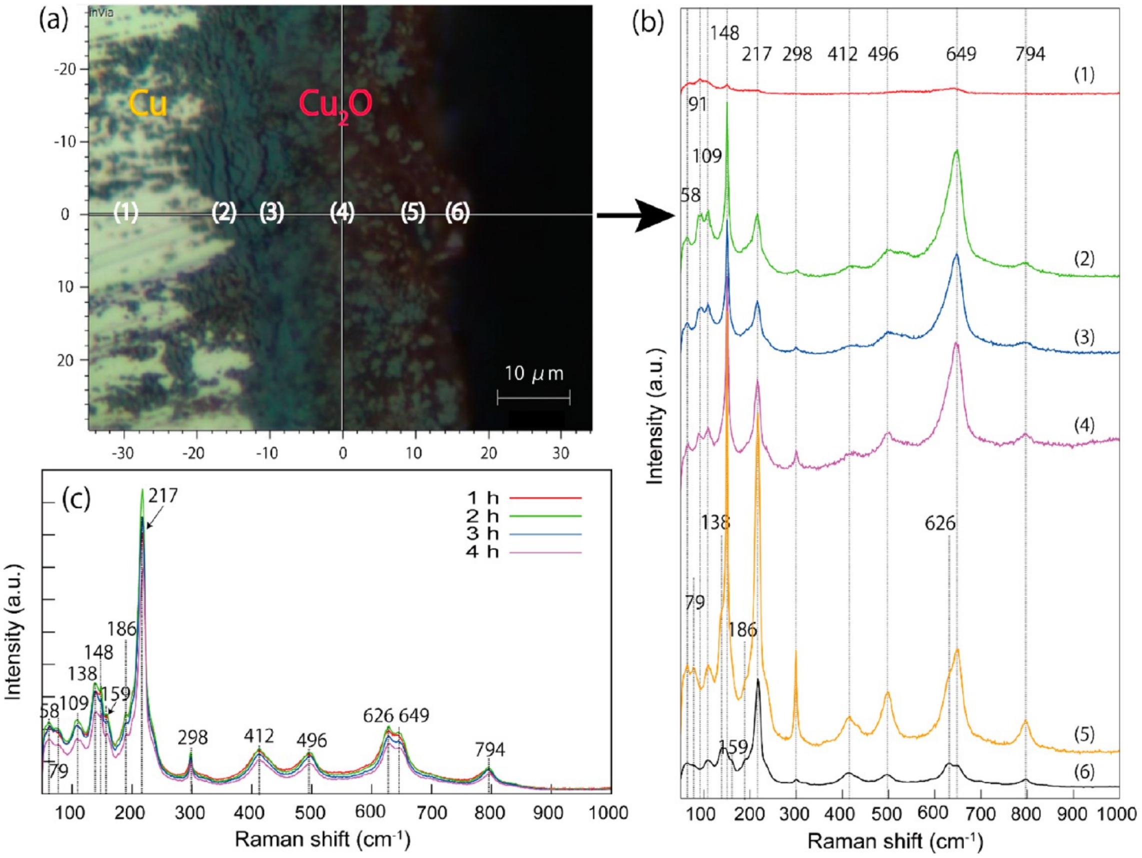

Figure 3. (a) Optical microscope image of the cross section of Cu_2O prepared at 500 °C for 3 h. The different positions along the central axis line of the cross section are marked by symbols (1), (2), (3), (4), (5), and (6), respectively. The Raman spectra taken at these positions are presented in part b. Part c shows the Raman spectra taken from the top surfaces of the Cu_2O samples prepared for the different annealing times of 1, 2, 3, and 4 h.

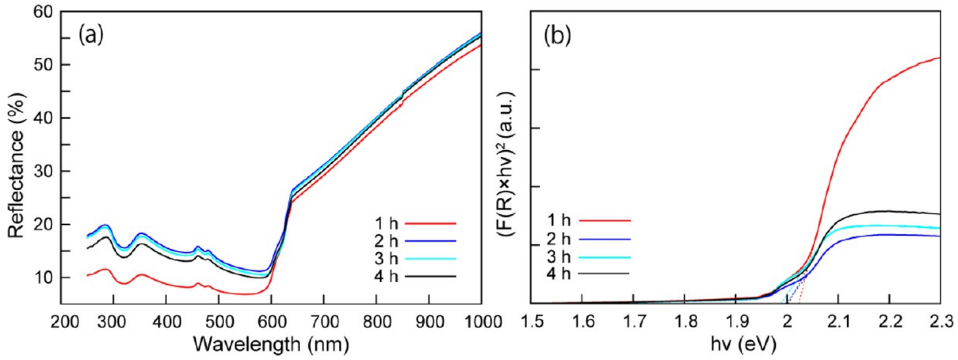

Figure 4. (a) Diffuse reflectance spectra and (b) calculated Kubelka–Munk function vs excitation energy plots for the 1, 2, 3, and 4 h annealed samples.

photons both in the Raman and in the IR spectra; the line observed at 794 cm^{-1} is attributed to IR active localized modes; the lines at 58, 109, and 298 cm^{-1} can be ascribed to Γ_{15}^-, Γ_{12}^-, and Γ_2^- band modes, respectively. All samples of Figure 3c exhibit the same characteristic Cu_2O peaks, indicating that all sample surfaces possess similar vibration modes within the penetration depth of the excitation laser. The apparent discrepancy between Raman scattering and XRD results is explained by greater sensitivity of Raman spectroscopy to the sample surface when compared with XRD analysis.[26,27]

Investigation into the phase depth profile is further conducted by Raman spectroscopy using spot measurements on a cross section of the 3 h annealed sample. Figure 3a shows an optical microscope image of the analyzed sample cross section with an estimated oxide thickness of 28.2 μm. Six spots marked by (1), (2), (3), (4), (5), and (6) from the Cu substrate to the Cu_2O thick film were chosen to probe phase change in the sample depth. The cross-section Raman spectra exhibit a continuous phase transformation from the outer region to the inner bulk region of Cu_2O, as shown in Figure 3b. In the Cu_2O region, the Raman spectrum from the outermost region (spot (6)) has the same characteristic bands as that of the top surface (Figure 3c). However, the Raman spectra taken from spots (2), (3), and (4) possessing the same characteristic bands are different from spot (6) by the absence of the peak at 91 cm^{-1} (Γ_{25}^-) and the presence of the peaks at 79 cm^{-1} (band modes), 138 cm^{-1}, 159 cm^{-1} (resonant modes), and 626 cm^{-1}. From spot (6) to spot (5), the very strong increase in the forbidden

148, 298, and 649 cm^{-1} lines and Raman-allowed features at 217 and 498 cm^{-1} are similar to the changes induced by ion-implantation reported by Powell et al.[28] The change of the 217 and 498 cm^{-1} is not clear at this stage. Since no structural damage from external ion implantation is involved in our samples, the increase in 148, 298, and 649 cm^{-1} peak intensities is likely caused by the relaxation of the symmetry selection rules due to the formation of defects (Cu vacancies or other point defects).[29−31] Also, the existence of the defects in this region leads to a deviation from stoichiometry and a change of the lattice constant of Cu_2O compared to the Cu_2O on the surface, in agreement with the results in XRD data. In summary, by combining XRD and Raman results, we conclude that for all samples the outer layer should be ascribed to Cu_2O-II while the underneath layer to Cu_2O-I, and the thickness of Cu_2O-II increased with annealing time.

3.3. Optical Properties. The optical properties of Cu_2O films measured by UV−vis diffuse reflectance spectra showed that the absorption intensity changes with annealing time, as presented in Figure 4a. The improved absorption in the region ranging from 250 to 600 nm for the 1 h annealed sample compared to the samples with larger crystals (2−4 h) may be attributed to its nanostructured morphology enhancing light trapping. The same effect was observed for the Cu_2O nanowire structures prepared under high vacuum (Figure S2c,d, Supporting Information). In order to evaluate the band gap energy of these films, $(F(R) \times h\nu)^2$ values for a direct band gap material[14] were plotted versus excitation energy where the absorption coefficient $F(R)$ was calculated according to the Kubelka−Munk (K−M) equation:[32,33]

$$F(R) = \frac{(1 - R)^2}{2R} \tag{1}$$

where R is the reflectance value of the thick Cu_2O layers. The samples annealed at 500 °C with different times have band gap energies between 1.99 and 2.02 eV, in agreement with the reported band gap energy for Cu_2O,[3,34] thus realizing efficient conversion of solar energy into chemical energy. The K−M plots of Figure 2b also reveal a shoulder in the band edge absorption at 1.95 eV, indicating the presence of doping levels. This result is confirmed later by the high carrier density found in Mott−Schottky analysis.

3.4. Photoelectrochemical Measurements. The photoelectrochemical (PEC) performances of the fabricated Cu_2O electrodes were evaluated in 0.5 M Na_2SO_4 (pH 6) electrolyte by linear sweep voltammetry (LSV) measurements under chopped AM 1.5G simulated sunlight at an irradiance of 100 mW/cm^2. A Pt wire and an Ag/AgCl electrode were used as the counter and reference electrodes, respectively. The scan rate was 10 mV/s, and the on−off interval was 2 s. The PEC responses of the Cu_2O electrodes prepared with different annealing times are presented in Figure 5. The photocurrent densities of −1.55, −4.07, −2.57, and −2.11 mA/cm^2 were obtained at 0 V/RHE for annealing times of 1, 2, 3, and 4 h, respectively. The photocurrents increased slowly for low external applied voltage (0.6−0.25 V vs RHE) and increased rapidly above 0.25 V vs RHE (the voltage sweep is from positive to negative). The best sample annealed for 2 h generated a photocurrent of −4.07 mA/cm^2 at 0 V vs RHE and reached a plateau at this voltage.

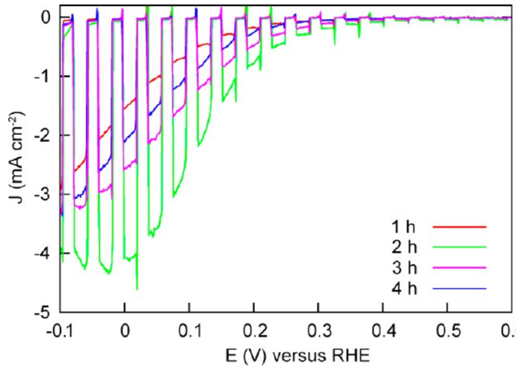

Figure 5. Photoelectrochemical responses of the electrodes prepared with the samples annealed for 1, 2, 3, and 4 h. The linear sweep voltammetry scans were conducted in 0.5 M Na_2SO_4 electrolyte (pH 6) under chopped AM 1.5G light illumination.

Above −0.1 V vs RHE, the dark current increased due to metal oxide reduction and/or water reduction. The photocurrent of the Cu_2O electrode (2 h) in our experiment was larger than the 2.28 mA/cm^2 at 0 V vs RHE of Cu_2O nanowires fabricated by thermal annealing of $Cu(OH)_2$ nanowires[10] and that of Cu_2O film prepared by electrodeposition which saturated at ∼2.4 mA/cm^2.[5] Similarly to previous reports,[5,7−10] a large proportion of the photocurrent is generated by the reduction of Cu_2O to Cu, as confirmed by the analysis of the Cu_2O electrode after water splitting shown in Figure S3 (Supporting Information). The XRD patterns (Figure S3b, Supporting Information) show an increase in the intensity of the Cu peaks of the Cu_2O electrode after the photoelectrochemical measurement compared to the original sample. The characteristic peaks of Cu_2O were found to shift from the Cu_2O-II (ICDD PDF card no. 9007497) to the Cu_2O-I (ICDD PDF card no. 1010941), thus suggesting that part of the Cu_2O-II was consumed and reduced to Cu metal. The nanoparticles formed on the surface of the electrode likely come from this Cu_2O reduction, as shown in Figure S3a (Supporting Information). Three times LSV scans of the Cu_2O samples taken under visible light (>420 nm, HOYA L42 cut-off filter) of a Xe lamp indicate an improved stability of the Cu_2O samples with the annealing time (Figure S4, Supporting Information). In a stability test, the photocurrent density of the Cu_2O electrodes decreased to about 0.11 ± 0.02 mA/cm^2 after 20 min under continuous illumination (Figure S5, Supporting Information). Although the high photocurrent of the Cu_2O film partially originated from the reduction of Cu_2O to Cu on the oxide surface, the large amount of carriers generated under illumination can be collected for efficient water splitting if the carriers can overcome the kinetic barrier at the oxide/electrolyte interface and react with protons. This can be achieved by coating n-type materials on the Cu_2O surface to generate a built-in field facilitating the transport of minority carriers into the electrolyte and obtain a more stable photocathode.[7,15,16] Thus, a protective layer is necessary for this structure for stable H_2 production in PEC cells.

3.5. Electrochemical Impedance. To know the flatband potential and charge carrier density, the Cu_2O electrodes were characterized by electrochemical impendence spectroscopy. The potential sweep was performed at a fixed frequency (1 kHz) with a scan speed of 10 mV/s. The flatband potential and charge carrier density can be extracted from the x-intercept and slope of the plot between the reciprocal of the square of capacitance per unit area, $1/C^2$, versus the applied voltage, V, according to the Mott−Schottky equation:[35]

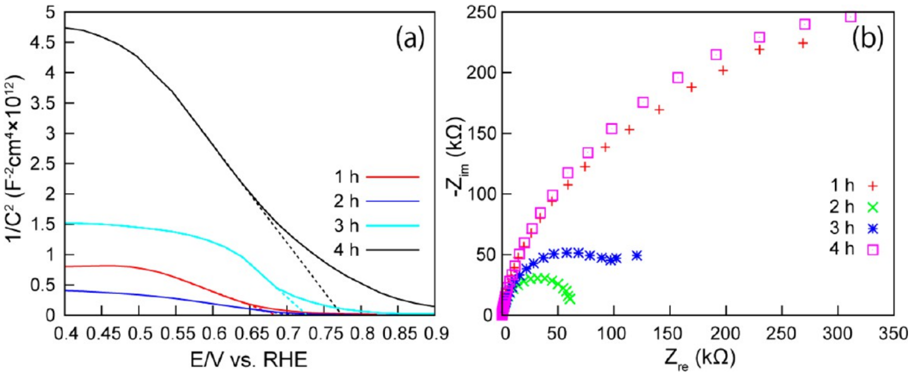

Figure 6. (a) Mott−Schottky analysis and (b) Nyquist plot taken with 0.01 M PBS solution (pH 7.4) of the samples annealed for 1, 2, 3, and 4 h. For Mott−Schottky measurements, the electrodes were scanned with a frequency of 1 kHz in the potential range of chemical stability. The Nyquist plot measurements were carried out at 0.43 V vs RHE by varying the frequency between 10 kHz to 1 Hz under dark conditions.

$$\frac{1}{C^2} = \left(\frac{2}{e\varepsilon\varepsilon_0 N_A}\right)\left[V - V_{fb} - \frac{k_B T}{e}\right] \tag{2}$$

where e is the electronic charge, ε is the relative permittivity of Cu_2O ($\varepsilon \sim 7.5$),[36] ε_0 is the permittivity of vacuum, k_B is Boltzmann's constant, T is the absolute temperature, and N_A is the carrier density. The active areas of the samples were accounted for by geometric consideration through a roughness factor.[37,38] The roughness factor f_r is estimated to be 3.2, 2.8, 1.75, and 1.7 for the 1, 2, 3, and 4 h annealed samples, respectively. Thus, from the slope k_{MS} of the lines, the carrier concentration N_A in the samples could be estimated from the equation:[38]

$$N_A = \frac{2}{e\varepsilon\varepsilon_0 k_{MS} f_r^{\,2}} \tag{3}$$

Figure 6 shows the Mott−Schottky plot for the Cu_2O electrodes taken in 0.01 M PBS electrolyte (pH 7.4). For the Cu_2O electrodes prepared with an annealing time from 1 to 4 h, the measured flatband potentials and charge carrier densities were 0.69, 0.71, 0.73, and 0.78 V vs RHE and 4.05×10^{17}, 1.36×10^{18}, 5.61×10^{17}, and 3.92×10^{17} cm^{-3}, respectively. The conduction bands are positioned at −1.24, −1.23, −1.18, and −1.13 V vs RHE, according to the above band gap energies and the following equation:

$$E_F - E_{VB} = k_B T \ln \frac{N_V}{N_A} \tag{4}$$

where N_A is the carrier density and N_V is the effective density of states in the valence band which can be expressed as

$$N_V = 2\left(\frac{2\pi m^* k_B T}{h^2}\right)^{3/2} \tag{5}$$

where $m^* = 0.58 m_0$ is taken as the effective hole mass.[36]

The conduction band position (1, 2, and 3 h) is more negative than those previously reported by Paracchino et al.[5] of −1.17 V vs RHE and de Jongh et al.[3] of −0.7 V vs RHE. Our relatively high conduction band may provide a larger driving force for hydrogen production. The carrier density in the fabricated Cu_2O films compared well with literature values having a higher value than the 5×10^{17} cm^{-3} and lower value than the 3.5×10^{20} cm^{-3} of the Cu_2O films prepared by electrodeposition.[5,39] The relatively high carrier density of the fabricated Cu_2O films may also contribute to the water splitting performance of our Cu_2O PEC cell. The Nyquist plots of Figure 6b were used to analyze the interfacial charge transfer process of the Cu_2O electrodes with the electrolyte. The measurement was carried out in the frequency range of 10 kHz to 1 Hz at a potential of 0.43 V vs RHE under dark conditions. The diameter of the semicircle is indicative of the interfacial charge transfer resistance, R_{ct}, across the electrode/electrolyte interface.[40] The 2 h sample showed the lowest R_{ct} value, and the resistance follows the order of R_{ct} (2 h) < R_{ct} (3 h) < R_{ct} (1 h) < R_{ct} (4 h).

It is well known that the crystal surface plays an important role in controlling catalytic activities by providing a surface and energetically favorable sites (terraces, steps, kinks, and vacancies) for chemical reactions.[22,41−44] In this report, the annealing time is found to increase the crystal size, thus decreasing the available surface for reaction, as well as decreasing surface irregularities, thus reducing the density of active sites for reaction. The decrease in the density of active sites also leads to a decrease in Cu vacancies in the vicinity of the sample surface which can serve as acceptors and thus should reduce the surface carrier density, as found in Figure 6a. Thus, the photocurrent decreases with the annealing time. We should note that the 1 h annealed sample is very unstable, as indicated by a color change from red to shallow black within a few days and the formation of a black dot under laser illumination, evidence for oxidization. This fast oxidation would not allow for correct estimation of the photocurrent, as the sample surface is likely transformed to CuO which has a low photocurrent. The 3 and 4 h annealed samples are far more stable but have only fair PEC performance due to the decrease in active catalytic sites (terraces, steps, and kinks) and increase of exposed low-index crystal facets {111}.[3,44] In contrast, the 2 h annealed sample has the largest photocurrent and a more stable state against surface oxidation in air, which are likely explained by the combination of high active site density and initial formation of {111} facets.

4. CONCLUSION

In this study, a new and low-cost fabrication method was introduced to synthesize Cu_2O microcrystalline films with high photoactivity. The two-step fabrication method consists of the synthesis of $Cu(OH)_2$ nanowires and their subsequent transformation into Cu_2O at 500 °C under a vacuum. By controlling the annealing time, the size of the crystals can be tuned and the preferential exposed facets {111} can be formed. Investigation into the samples' depth crystal properties reveals that the outer and inner regions of the oxide layer were composed of two types of cubic Cu_2O with different lattice constants, as evidenced by XRD and Raman analysis. The conduction band values of −1.24, −1.23, −1.18, and −1.13 V vs RHE and the large carrier densities of 4.05×10^{17}, 1.36×10^{18}, 5.61×10^{17}, and 3.92×10^{17} cm^{-3} for the 1−4 h samples presumably contributed to the high photocurrents of −1.55, −4.07, −2.57, and −2.11 mA/cm^2 at 0 V vs RHE under AM 1.5G illumination, respectively. The next challenge is to stabilize the bare Cu_2O electrode with appropriate protective layers as well as load proper H_2 evolution catalysts on the Cu_2O surface to reduce water to hydrogen more efficiently.

■ ASSOCIATED CONTENT

Ⓢ Supporting Information

Characterization data for $Cu(OH)_2$ nanowires, high vacuum annealed Cu_2O nanowires, and Cu_2O electrodes after PEC measurements. Stability measurements of the Cu_2O microcrystalline films. This material is available free of charge via the Internet at http://pubs.acs.org.

■ AUTHOR INFORMATION

Corresponding Author

*E-mail: jean@mech.t.u-tokyo.ac.jp.

Notes

The authors declare no competing financial interest.

■ ACKNOWLEDGMENTS

C.L. thanks the China Scholarship Council (201206230077). The authors thank Dr. Miao Zhong for guidance with XRD and FE-SEM. The XRD analysis was conducted in the Research Hub for Advanced Nano Characterization, The University of Tokyo, supported by MEXT, Japan.

■ REFERENCES

(1) Peterson, N. L.; Wiley, C. L. *J. Phys. Chem. Solids* **1984**, *45*, 281−294.
(2) Mrowec, S.; Stokłosa, A. *Oxid. Met.* **1971**, *3*, 291−311.
(3) de Jongh, P. E.; Vanmaekelbergh, D.; Kelly, J. J. *J. Electrochem. Soc.* **2000**, *147*, 486−489.
(4) de Jongh, P. E.; Vanmaekelbergh, D.; Kelly, J. J. *Chem. Commun.* **1999**, 1069−1070.
(5) Paracchino, A.; Brauer, J. C.; Moser, J.-E.; Thimsen, E.; Graetzel, M. *J. Phys. Chem. C* **2012**, *116*, 7341−7350.
(6) Siripala, W.; Ivanovskaya, A.; Jaramillo, T. F.; Baeck, S.-H.; McFarland, E. W. *Sol. Energy Mater. Sol. Cells* **2003**, *77*, 229−237.
(7) Paracchino, A.; Laporte, V.; Sivula, K.; Grätzel, M.; Thimsen, E. *Nat. Mater.* **2011**, *10*, 456−461.
(8) Qian, F.; Wang, G. M.; Li, Y. *Nano Lett.* **2010**, *10*, 4686−4691.
(9) Lin, C.-Y.; Lai, Y.-H.; Merscha, D.; Reisner, E. *Chem. Sci.* **2012**, *3*, 3482−3487.
(10) Zhang, Z. H.; Dua, R.; Zhang, L. B.; Zhu, H. B.; Zhang, H. N.; Wang, P. *ACS Nano* **2013**, *7*, 1709−1717.
(11) Li, C. W.; Kanan, M. W. *J. Am. Chem. Soc.* **2012**, *134*, 7231−7234.
(12) Mittiga, A.; Salza, E.; Sarto, F.; Tucci, M.; Vasanthi, R. *Appl. Phys. Lett.* **2006**, *88*, 163502.
(13) Xiang, C. X.; Kimball, G. M.; Grimm, R. L.; Brunschwig, B. S.; Atwater, H. A.; Lewis, N. S. *Energy Environ. Sci.* **2011**, *4*, 1311−1318.
(14) Hu, C.-C.; Nian, J.-N.; Teng, H. *Sol. Energy Mater. Sol. Cells* **2008**, *92*, 1071−1076.
(15) Paracchino, A.; Mathews, N.; Hisatomi, T.; Stefik, M.; Tilley, S. D.; Grätzel, M. *Energy Environ. Sci.* **2012**, *5*, 8673−8681.
(16) Tilley, S. D.; Schreier, M.; Azevedo, J.; Stefik, M.; Grätzel, M. *Adv. Funct. Mater.* **2013**, DOI: 10.1002/adfm201301106.
(17) Zhang, W.; Wen, X.; Yang, S.; Berta, Y.; Wang, Z. L. *Adv. Mater.* **2003**, *15*, 822−825.
(18) Lu, C. H.; Qi, L. M.; Yang, J. H.; Zhang, D. Y.; Wu, N. Z.; Ma, J. M. *J. Phys. Chem. B* **2004**, *108*, 17825−17831.
(19) Tsiranovits, Ch.; Antonopulos, J. G.; Stoemenos, J. *Thin Solid Films* **1980**, *71*, 133.
(20) Wagner, C.; Grunewald, K. *Z. Phys. Chem.* **1938**, *B40*, 455.
(21) Haugsrud, R. *J. Electrochem. Soc.* **2002**, *149*, B14−B21.
(22) Quan, Z. W; Wang, Y. X.; Fang, J. Y. *Acc. Chem. Res.* **2013**, *46*, 191−202.
(23) Zhu, Y. F.; Mimura, K.; Isshiki, M. *Mater. Trans.* **2002**, *43*, 2173−2176.
(24) Gonçalves, A. M. B.; Campos, L. C.; Ferlauto, A. S.; Lacerda, R. G. *J. Appl. Phys.* **2009**, *106*, 034303.
(25) Reydellet, J.; Balkanski, M.; Trivich, D. *Phys. Status Solidi B* **1972**, *52*, 175−185.
(26) Fan, F. T.; Feng, Z. C.; Li, C. *Acc. Chem. Res.* **2010**, *43*, 378−387.
(27) Zhang, J.; Li, M. J.; Feng, Z. C.; Chen, J.; Li, C. *J. Phys. Chem. B* **2006**, *110*, 927−935.
(28) Powell, D.; Compaan, A.; Macdonald, J. R. *Phys. Rev. B* **1975**, *12*, 20−25.
(29) Compaan, A. *Solid State Commun.* **1975**, *16*, 293−296.
(30) Arora, A. K.; Ramdas, A. K. *Phys. Rev. B* **1987**, *35*, 4345−4350.
(31) Berg, R. S.; Yu, P. Y. *Phys. Rev. B* **1986**, *33*, 7349−7352.
(32) Wilkinson, F. *J. Chem. Soc., Faraday Trans.* **1986**, *2*, 2073−2081.
(33) Oelkrug, D.; Honnen, W.; Wilkinson, F.; Willsher, C. J. *J. Chem. Soc., Faraday Trans.* **1987**, *2*, 2081−2095.
(34) Rakhshani, A. E. *Solid-State Electron* **1986**, *29*, 7−17.
(35) Cardon, F.; Gomes, W. P. *J. Phys. D: Appl. Phys.* **1978**, *11*, L63.
(36) Hodby, J. W.; Jenkins, T. E.; Schwa, C.; Tamura, H.; Trivich, D. *J. Phys. C: Solid State Phys.* **1976**, *9*, 1429.
(37) Formal, F. L.; Tétreault, N.; Cornuz, M.; Moehl, T.; Grätzel, M.; Sivula, K. *Chem. Sci.* **2011**, *2*, 737−743.
(38) Li, Y. B.; Zhang, L.; Torres-Pardo, A.; González-Calbet, J. M.; Ma, Y. H.; Oleynikov, P.; Terasaki, O.; Asahina, S.; Shima, M.; Cha, D. K.; Zhao, L.; Takanabe, K.; Kubota, J.; Domen, K. *Nat. Commun.* **2013**, *4*, 2566.
(39) Nakaoka, K.; Ueyama, J.; Ogura, K. *J. Electrochem. Soc.* **2004**, *151*, C661−C665.
(40) Hong, S. J.; Lee, S.; Jang, J. S.; Lee, J. S. *Energy Environ. Sci.* **2011**, *4*, 1781−1787.
(41) Shaikhutdinov, S. K.; Meyer, R.; Naschitzki, M.; Bäumer, M.; Freund, H.-J. *Catal. Lett.* **2003**, *86*, 211−219.
(42) Štrbac, S.; Adžić, R. R. *J. Electroanal. Chem.* **1996**, *403*, 169−181.
(43) Gong, X. Q.; Selloni, A.; Dulub, O.; Jacobson, P.; Diebold, U. *J. Am. Chem. Soc.* **2008**, *130*, 370−381.
(44) Sun, S. D.; Song, X. P.; Sun, Y. X.; Deng, D. C.; Yang, Z. M. *Catal. Sci. Technol.* **2012**, *2*, 925−930.